



ORIGINAL RESEARCH ARTICLE

Microstructure and Properties of Laser Surface Melted AISI 316L Stainless Steel

Sharath Anishetty, Tapas Bera, Swapan Kumar Karak, Jyotsna Dutta Majumdar, and Indranil Manna

Submitted: 18 June 2023 / Revised: 25 February 2024 / Accepted: 7 March 2024

The present study aims to understand the influence of laser parameters (applied power density and scan speed) on microstructure, surface mechanical (microhardness and wear resistance), and electrochemical (corrosion resistance) properties of AISI 316L stainless steel following laser surface melting (LSM), conducted using a 6.6 kW continuous wave diode laser with the applied power density and scan speed ranging from 58.98 to 88.46 W/mm² and 20 to 80 mm/s, respectively. Detailed characterization included microstructure investigation, composition analysis, phase determination, and assessment of wear and corrosion resistance. The melt zone microstructure mainly comprises dendrites with the secondary arm spacing systematically varying with laser parameters. With increase in laser power density, cumulative lattice strain, dislocation density, and residual stress increased. The relationship between these properties and scan speed is just the opposite. Microhardness of the melt zone varied between 180 and 336 VHN, with higher values obtained either at higher laser power density or lower scan speed. Similarly, wear volume and wear rate after LSM also vary with the laser parameters. Detailed microstructural analysis of the worn surface was carried out to study the mechanism of wear. Interestingly, LSM recorded a corrosion resistance better than that in as-received conditions which systematically varies with the LSM parameters. Orientation imaging by electron backscattered diffraction analysis suggested that LSM with 88.46 W/mm² power density and 20 mm/s scan speed developed a lower area fraction of high-angle grain boundaries and orientation mismatch and, hence, offered highest corrosion resistance in a 3.56 wt.% NaCl solution.

Keywords austenitic stainless steel, corrosion, hardness, laser surface melting, microstructure, wear

1. Introduction

AISI 316L austenitic stainless steel offers an attractive combination of moderate strength, high toughness, moderate wear resistance, and good corrosion resistance. As a result, this grade of steel is widely used as structural components in automotive, marine, chemical, petrochemical, and biomedical sectors (Ref 1, 2). However, this steel is not reliable in abrasive wear and aggressive environments (especially fluoride containing environments). Appropriate surface engineering interventions are known to improve resistance to wear and corrosion, which are mostly surface-dependent degradations (Ref 3-5). Indeed, mechanical and electrochemical properties of AISI 316L stainless steel have been enhanced by various surface engineering techniques in the past, including physical (PVD) or

chemical vapor deposition (CVD), electrodeposition, surface alloying, and hard facing. For use in proton exchange membrane fuel cells (PEMFCs) and bipolar plates, Jannat et al. (Ref 6) used cathodic arc evaporation based PVD to create a multi-layer nanometric Ti/TiN coating. Multilayered coatings of nanometric CrN/ZrN and CrN/CrAlN on stainless steel for the same PEMFCs were successfully developed using a similar thin film deposition process (Ref 7). Ali et al. (Ref 8) demonstrated that electron beam-assisted PVD is an effective method to deposit thin film with controlled layer thickness. In order to increase the biocompatibility of stainless steel, Zhu et al. (Ref 9) developed a diamond-like carbon coating on the material using microwave-assisted plasma-aided CVD. The effect of preheating temperature on the microstructure and degree of hardening of tungsten carbide coating was studied by Sabzi et al. (Ref 10) using hot filament-assisted CVD. In another investigation, titanium nitride was deposited on stainless steel for surgical instruments by CVD using a gas mixture of TiCl₄, H₂ and N₂ (Ref 11). Garcia et al. (Ref 12) developed CTS (chitosan)/HAp composite coatings on AISI 316L stainless steel substrate by electrodeposition process and studied its tribological behavior. On stainless steel, pulse electroplating of chromium-palladium alloy films showed excellent corrosion resistance and good adhesive strength in boiling H₂SO₄, acetic-formic acid mixture, and simulated proton exchange membrane fuel cell environments (Ref 13). Laser surface alloying (LSA) of TiC, Ti + SiC, SiC, and C increased the surface hardness of stainless steel by precipitating hard carbides during solidification (Ref 14). A composite hydroxyapatite-titanium oxide ceramic layer was developed by LSA to increase the biocompatibility of the same stainless steel (Ref 15).

Sharath Anishetty, Tapas Bera, and Jyotsna Dutta Majumdar, Department of Metallurgical and Materials Engineering, Indian Institute of Technology Kharagpur, Kharagpur, West Bengal 721302, India; **Swapan Kumar Karak**, Department of Metallurgical and Materials Engineering, National Institute of Technology Rourkela, Rourkela, Odisha 769008, India; and **Indranil Manna**, Department of Metallurgical and Materials Engineering, Indian Institute of Technology Kharagpur, Kharagpur, West Bengal 721302, India; and Birla Institute of Technology, Mesra, Ranchi, Jharkhand 835215, India. Contact e-mail: imanna@metal.iitkgp.ernet.in.

Among different surface engineering techniques employed, LSM is a relatively simpler method involving melting the surface of the components up to a limited depth by high-power laser irradiation followed by rapid solidification to form a significantly refined microstructure and yield marked improvement in corrosion resistance property, resulting from the combined refinement and uniformity of microstructure and homogeneity of composition (Ref 16-18). LSM offers additional advantages of precise control of the microstructure, melt depth, heat-affected zone, rapid processing speed, and easy applicability to alloys with a wide range of melting points and other thermo-physical properties (Ref 19). In the past, LSM was successfully utilized to increase the surface hardness of tool steel (Ref 20, 21), low alloy steel (Ref 22), and gray and nodular cast irons (Ref 23). It has also been observed that a post-laser melting heat treatment operation may improve the hardness of high chromium steel (Ref 24). Corrosion and wear resistance of Al and other metallic alloys were also reported to be improved by LSM (Ref 25-28). Several works have also been conducted on LSM of AISI 304 stainless steel (Ref 29, 30), AISI 304L stainless steel (Ref 31, 32), AISI 316 stainless steel (Ref 33), AISI 316L stainless steel (Ref 34-39) and martensitic (Ref 40), and duplex stainless steel (Ref 41) for improving the surface-dependent properties. Notable studies in this regard include studies by Cui et al. (Ref 29) on LSM of AISI 304 stainless steel with Nd:YAG laser, leading to improvement in hardness and wear resistance. Jafar et al. (Ref 30) reported the dissolution of chromium carbide by LSM of AISI 304 stainless steel and the formation of refined and homogeneous microstructure. In another study, Mahanti Ghoshal et al. (Ref 31) reported an improvement in the pitting corrosion resistance of AISI 304L stainless steel using Nd:YAG laser, which was attributed to the elimination of inclusions and impurity segregation at the grain boundary. Akgun et al. (Ref 32) reported a 15% lowering of Mn content due to LSM of AISI 304L stainless steel. Parvathavarthini et al. (Ref 33) reported on the desensitization of AISI 316 stainless steel by LSM, which was attributed to the complete dissolution of $M_{23}C_6$ precipitates and suppression of reprecipitated due to rapid quenching. An improvement in hardness and cavitation corrosion resistance of austenitic stainless steels S31603, S30400 and super duplex stainless steel S32760 by LSM using continuous wave Nd:YAG laser were earlier reported by Kwok et al. (Ref 34) and correlated with the microstructure. Ghorbani et al. (Ref 35) demonstrated the possibility of improving the surface quality of selective laser melted AISI 316L stainless steel by LSM under optimum parameters. Vilchez et al. (Ref 36) studied the effect of LSM of AISI 316L stainless steel welded joints on its corrosion performance. Balla et al. (Ref 37) studied the effect of LSM of AISI 316L stainless steel on its corrosion resistance (in Hank's solution), wettability, and cell adherence and reported an improvement of those properties by LSM. However, the influence of process parameters on microstructure, microhardness, wear, and corrosion resistance was not studied in detail. Kumar et al. (Ref 38) did an extensive study on the LSM of AISI 316L stainless steel using Nd:YAG laser in Ar and N_2 atmosphere and reported an improvement in microstructure, microhardness, wear, and corrosion resistance (in Hank's solution) due to LSM. However, the mechanism of corrosion was not studied in detail. In this regard, it may be noted that a detailed investigation of the effect of microstructure (especially the grain size and its distribution, nature of grain boundaries, strain, and grain orientation) on the kinetics

of wear and corrosion due to LSM of AISI 316L stainless steel was not reported earlier. Hence, in this study, an attempt has been made to understand the effect of laser parameters on the surface microstructure, wear resistance, and corrosion resistance of laser surface melted AISI 316L stainless steel developed by diode laser and establish a structure-property-process parameter correlation. The micro-mechanism of corrosion enhancement has also been established through a detailed EBSD mapping. In addition, the optimum process parameter for maximum improvement in wear and corrosion resistance has been established.

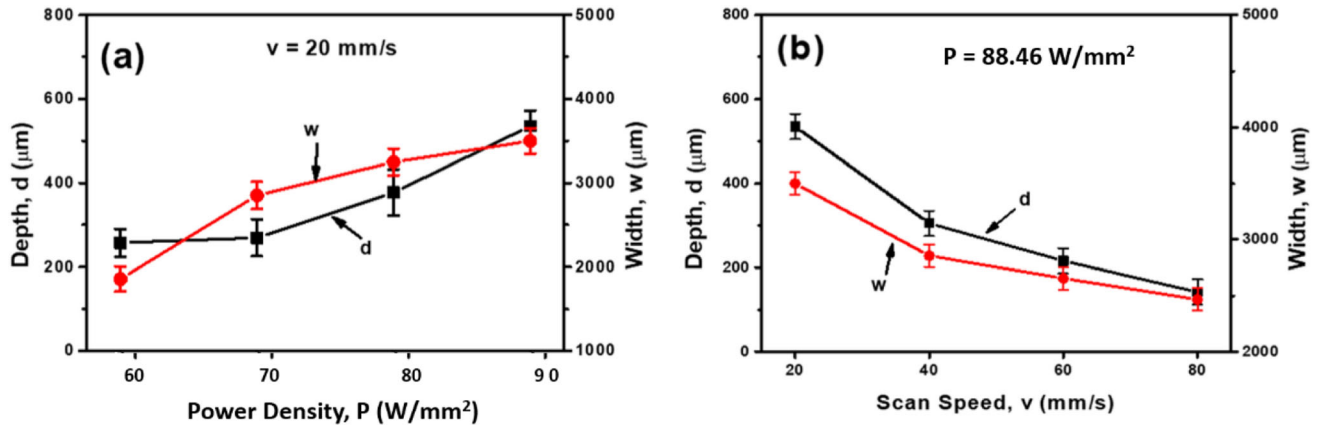
2. Experimental Procedure

In this study, AISI 316L stainless steel (composition: 68.5 Fe, 17.5 Cr, 9.7 Ni, 2.2 Mo, 1.6 Mn, and 0.5 Si, all in wt.%) sheet was cut to dimensions of $50 \times 50 \times 5$ mm and used as a substrate for LSM. Prior to laser irradiation, sandblasting was applied to clean and increase absorptivity on the substrate surface. LSM was carried out using a 6.6 kW (maximum power) continuous wave diode laser (wavelength of 1000 nm) with a 3.6 mm beam diameter (at focus) with a Gaussian intensity distribution profile covered by an argon shroud. In this regard, it may be noted that all LSM experiments were conducted with the same configuration with 30-40% overlap between successive tracks to maintain uniformity and comparability, and even out the differences in the depth of melting. A similar beam was also used and reported for LSM of metallic materials in the past (Ref 42, 43). The range of process parameters (applied power density: 58.98-88.46 W/mm², scan speed: 20-80 mm/s, and 3.6 mm beam diameter) used in the present study were selected based on several trial runs aimed to identify the suitable process window for the formation of defect-free melt zones with minimum surface roughness. In this regard, it may be noted that similar parameters were also reported earlier for laser surface melting of AISI 316L stainless steel. Notable reports in this regard include (i) LSM of AISI 316L stainless steel using laser power of 1350 W, scan speed of 21 mm/s, and beam diameter of 1.7 mm by Kwok et al. (Ref 34), (ii) LSM of AISI 316L stainless steel using Nd:YAG laser with 200 W applied power, 10 mm/s scan speed, and beam diameter of 361 μ m by Vilchez et al. (Ref 36) and (iii) LSM of AISI 316L stainless steel using Nd:YAG laser with 750-1000 W laser power, 0.05-0.1 m/s scan speed, and 4 mm beam diameter by Kumar et al. (Ref 38). In addition, a systematic study showed that a laser beam diameter higher than 3.6 mm produced distortion of the beam shape with an inhomogeneous distribution of beam energy across the beam diameter in the present laser system. Since the focus was more on the improvement of surface-dependent properties than studying the effect of beam diameter and shape, all studies were conducted only with this same beam diameter of 3.6 mm.

Table 1 shows the laser parameters used in the present study. Following LSM, the microstructure and micro-composition of the top surface and cross-sectional plane were studied using a scanning electron microscope (SEM, Model: SUPRA 40, Make: Zeiss, Germany) coupled with an energy dispersive x-ray spectroscope (EDS). Phase along with micro-strain and crystallite size was determined using x-ray diffraction (XRD, D8 Advanced, Bruker, Germany). Microhardness was measured by Vickers microhardness tester (Walter UHL, VMHT) at 50 gf of

Table 1 Summary of experimental parameters used in the present study

Sl. No.	Power, W	Beam diameter, mm	Power density, P , W/mm ²	Scan speed, v , mm/s	Wavelength, nm
1	600	3.6	58.98	20, 40, 60, 80	1000
2	700		68.81		
3	800		78.63		
4	900		88.46		

**Fig. 1** Variation of depth and width of melt zone with (a) applied power density at constant scan speed of 20 mm/s and (b) scan speed at a constant power density of 88.46 W/mm²

load applied for 10 s dwell time. The nano-mechanical characteristics of the as-received and LSM samples were determined using a nanoindenter (Hysitron-TI950 Triboindenter) equipped with a Berkovich tip applying 20 mN maximum load for 10 s of loading and unloading period. Wear resistance property was then assessed utilizing ball-on-disk wear testing equipment in the fretting wear mode using a tungsten carbide ball, 10 N of load, and 10 Hz of oscillation frequency. The kinetics of wear were analyzed in terms of variation in cumulative wear depth over time by using the Rtec machine and dedicated software. Also, a time-dependent evaluation of the coefficient of friction was carried out using the same methodology. Following wear tests, microstructural damages were assessed by an SEM. Electron backscattered diffraction analysis (EBSD) was carried out with samples in as-received condition and after LSM. Using Ag/AgCl standard electrode as a reference electrode and its counter electrode as platinum, the potentiodynamic polarization studies were conducted to electrochemically analyze the corrosion resistance property at an applied voltage ranging from -0.5 to 1.0 V and scan rate of 0.001 V/s in 3.56 weight percent NaCl solution at a pH of 6.1 using a standard potentiostat/galvanostat (Model: Autolab PGSTAT302N, AUT87037 Make: Metrohm, The Netherlands). The corrosion rate was determined using Tafel's extrapolation approach. Finally, post-corrosion microstructural analysis was conducted using an SEM after immersing the sample for 72 h in 3.56 wt.% NaCl solution.

3. Results and Discussion

Figure 1(a) and (b) shows the variation of vertical melt depth and lateral width of the laser tracks developed by variation of (a) P at $v = 20$ mm/s and (b) v at $P = 88.46$ W/

mm², respectively. It is apparent that both the depth and width of the surface melt zone increase with P but decrease with v , respectively. These effects reflect that, as normally expected, heat input and degree of laser energy coupling on the metallic surface increase as P increases but v decreases, respectively. The P and v combination is so selected that the maximum temperature developed during laser irradiation remains below the boiling temperature of the substrate to prevent surface evaporation and crater formation. The variation of heat input with P and v was discussed earlier in detail by theoretical modeling and experimental validation (Ref 44, 45).

Figure 2(a), (b) and (c) shows the (a) SEM image, (b) elemental profile derived from EDS analysis, and (c) XRD profile of as-received AISI 316L stainless steel, revealing the presence of coarse grain equiaxed morphology with average grain size varying from 20 to 30 μm and the arrows showing the presence of twins (cf. Fig. 2a) in between. The twins are usually observed in the microstructure possibly due to prior deformation and annealing (Ref 46). From Fig. 2(a), it may further be noted that the grains are contaminant-free, and there is no evidence of any precipitate. From Fig. 2(b), it may be noted that Fe, Cr, Ni, Mn, and Si are present in the microstructure with an average composition of 68.5 wt.% Fe, 17.5 wt.% Cr, 9.7 wt.% Ni, 2.2 wt.% Mo, 1.6 wt.% Mn, and 0.5 wt.% Si. However, there was no signature of the presence of measurable S in the EDS profile. Figure 2(c) further reveals that there is the presence of only gamma peaks in the XRD profile. However, there is no signature of oxide or MnS in the x-ray diffraction profile. Hence, AISI 316L stainless steel used in the present study is contaminant-free with no signature of any other phase.

Following LSM, it is known that surface roughness, depth of melt zone, microstructure, morphology, phase, and composition across the melt zone largely determine the surface-

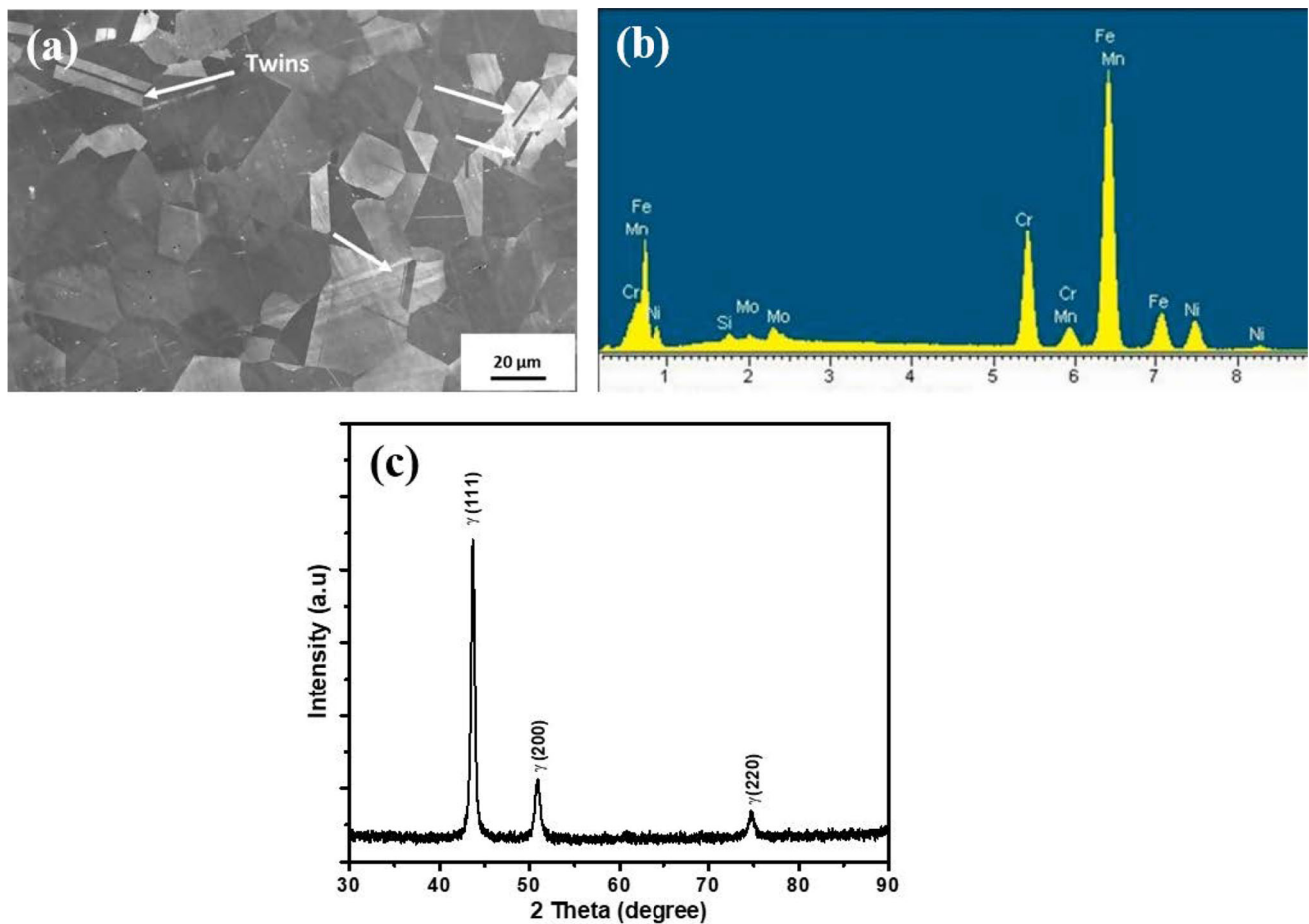


Fig. 2 (a) SEM image, (b) elemental profile derived from EDS analysis, and (c) XRD profiles of as-received AISI 316L stainless steel

dependent mechanical and functional properties. In the current experiment, characterization of the above-mentioned parameters was undertaken and correlated with laser and process parameters. Figure 3(a), (b), (c), and (d) shows that the SEM image of the (a) substrate following LSM with $P = 58.98 \text{ W/mm}^2$ and $v = 20 \text{ mm/s}$ along with the same at higher magnification of (b) zone 1, (c) zone 2, and (d) zone 3 (as marked in Fig. 3a), respectively. Figure 3(a) shows the cross section of the melt pool of a single track, as a result of which the thickness is not uniform all throughout. However, to ensure a melt pool with minimum thickness, 25% overlapping was applied. Figure 3(a) reveals that the melt zone underwent typical directional solidification with columnar-dendritic morphology growing from the bottom (substrate-melt zone interface) to the top. The top surface, examined at high magnification, reveals almost equiaxed cellular morphology, with cells ranging in size from 3 to 10 μm . Similar equiaxed morphology is commonly observed after LSM with different process parameters (Ref 38, 47). The cellular morphology on the top surface originates from long columnar or dendritic growth from the bottom. This is corroborated by Fig. 3(b) and (c) that confirm the presence of columnar morphology in the middle of the melt zone that gradually transforms into a columnar-dendritic structure near the top surface and eventually into nearly equiaxed cellular distribution at the top surface. The width of the near-surface equiaxed region, columnar-dendritic region, and columnar region varied with thermal history and, hence, laser parameters.

In addition, it was observed that the grain size, secondary dendrite arm spacing (SDAS), and inter-columnar width were also affected by the applied laser parameters.

Figure 4(a), (b), and (c) shows the scanning electron micrographs of the top surface of laser surface melted AISI 316L stainless steel lased at (a) applied power density of 58.98 W/mm^2 , scan speed of 20 mm/s , (b) applied power density of 88.46 W/mm^2 , scan speed of 20 mm/s , and (c) applied power density of 88.46 W/mm^2 , scan speed of 80 mm/s . From Fig. 4(a), it may be noted that the microstructure of the laser surface melted AISI 316L stainless steel consists of predominantly equiaxed morphology with an average grain size of 10-15 μm . From the close comparison of Fig. 4(a) and (b), it may be noted that, with an increase in applied power density, there is a significant refinement of microstructure with average grain size varying from 2 to 4 μm . Similar variation of microstructure with applied power density was reported earlier by Rajan et al. (Ref 48). On the other hand, with an increase in scan speed, there is marginal coarsening of microstructure (Fig. 4b vis-à-vis Fig. 4c). The variation of grain size with applied power density and scan speed is summarized in Fig. 5. The decrease in grain size with an increase in applied power density is attributed to rapid cooling associated with an increase in applied power density. On the other hand, with an increase in scan speed, the grain size is coarsened because of the lower cooling rate due to availability of less time for convective dominated heat transfer during solidification. The effect of individual parameters on the

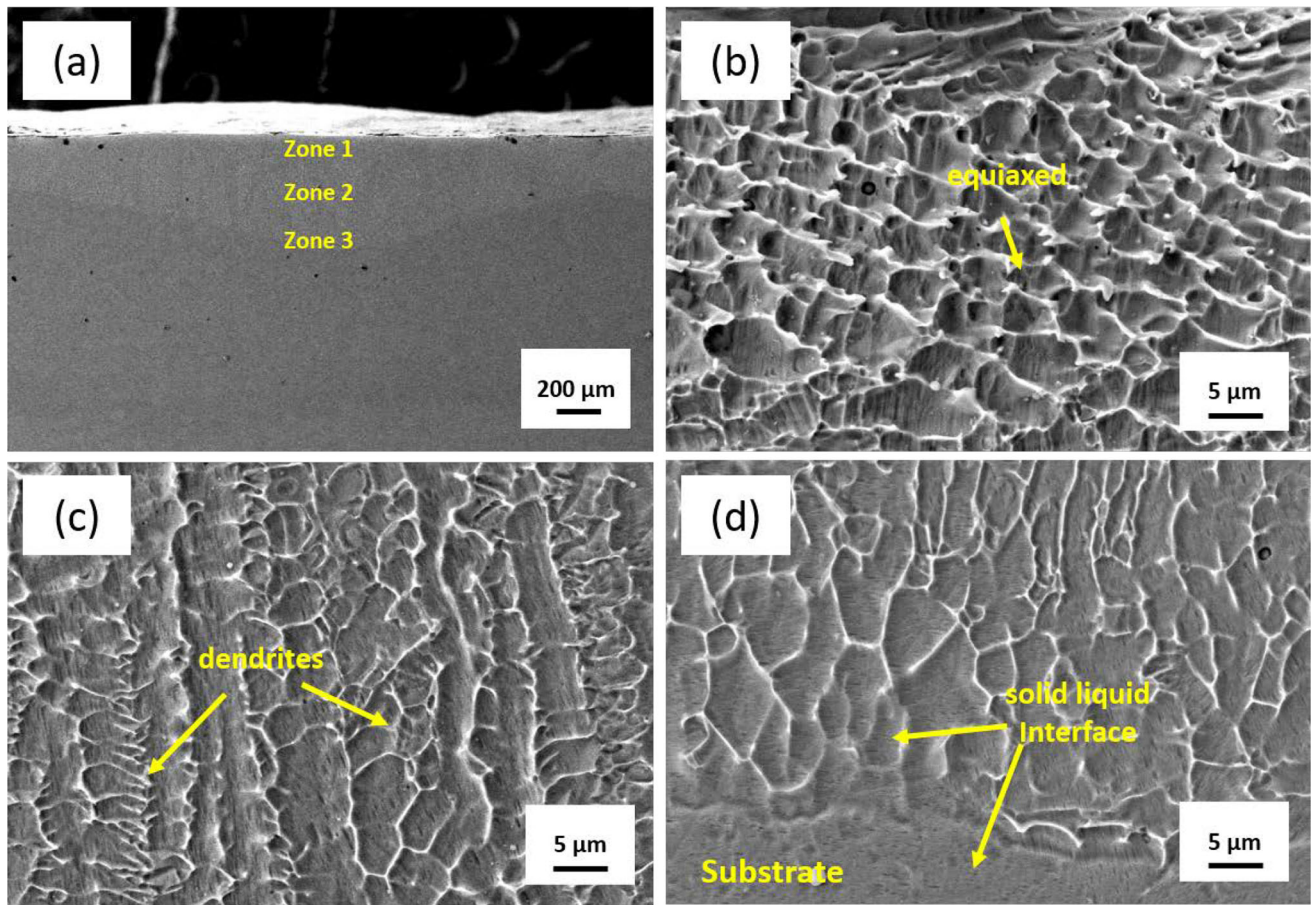


Fig. 3 SEM images of the (a) cross section, (b) top surface (zone 1), (c) intermediate (zone 2), and (d) solid–liquid interface (zone 3) of laser surface melted specimen lased with $P = 88.46 \text{ W/mm}^2$ and $v = 20 \text{ mm/s}$

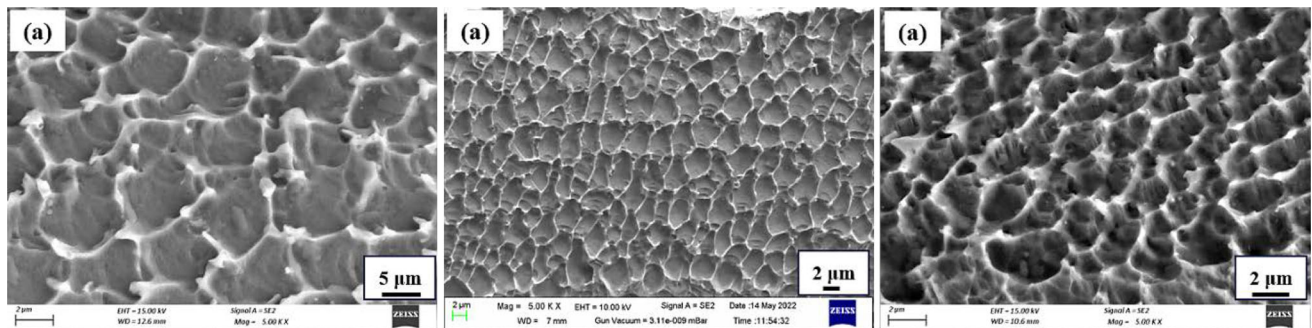


Fig. 4 SEM images of the top surface of laser surface melted AISI 316L stainless steel processed with (a) $P = 58.98 \text{ W/mm}^2$ at $v = 20 \text{ mm/s}$, (b) 88.46 W/mm^2 at $v = 20 \text{ mm/s}$ and (c) 88.46 W/mm^2 at $v = 80 \text{ mm/s}$

grain size for the whole set of samples is summarized in Fig. 5(a). In this regard, it may also be noted that Fig. 5(a) represents the equiaxed grain size/secondary dendritic arm spacing/columnar grain size of the whole set of parameters of laser processing applied in the present study.

Figure 5(a) and (b) illustrates the influence of applied power density and scan speed on (a) equiaxed grain size/secondary dendritic arm spacing/columnar grain size and (b) width of individual morphology in the microstructure after LSM. From Fig. 5(a), it may be noted that there is a systematic decrease in equiaxed grain size/secondary dendritic arm spacing/columnar grain size with an increase in applied power density and

increase of the same with an increase in scan speed which is also evident from the microstructural features, as discussed in Fig. 4. In this regard, it may be noted that columnar morphology is usually observed at the solid–liquid interface followed by dendritic and then equiaxed morphology at the near-surface region. Hence, the similar trend of the variation in equiaxed grain size/secondary dendritic arm spacing/columnar width confirms that the cooling rate with depth is the same for the present set of laser parameters. From Fig. 5(b), it may be noted that the thickness of the equiaxed zone formed on the surface increases with an increase in applied power density up to 78.63 W/mm^2 , followed by which it decreases marginally at

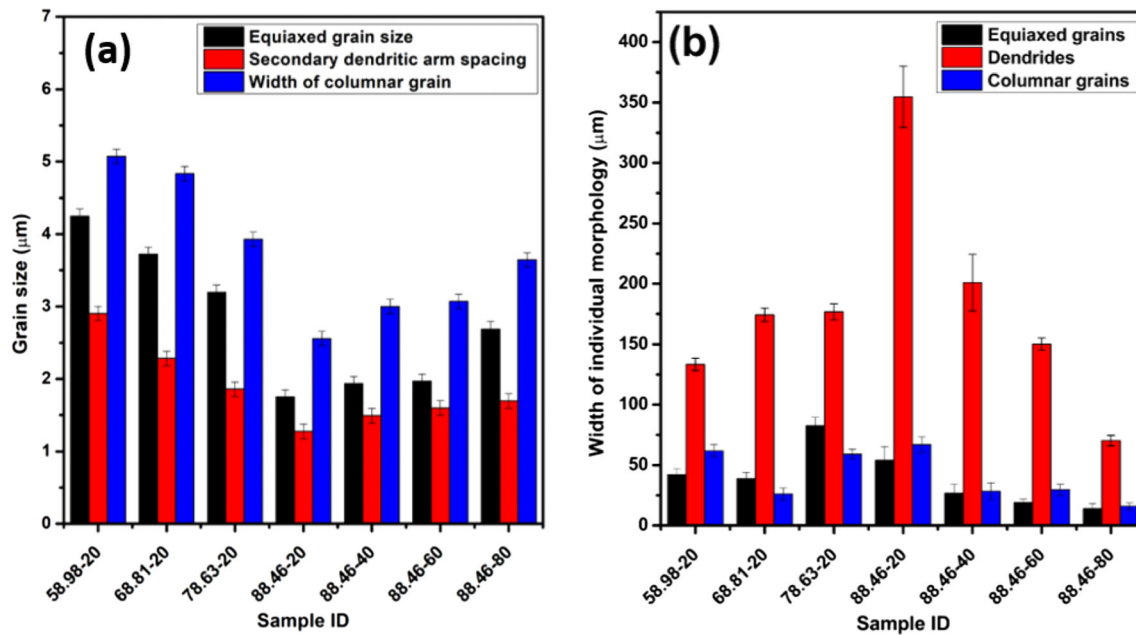


Fig. 5 Variation of (a) equiaxed grain size/secondary dendritic arm spacing/columnar grain size and (b) width of individual morphology in the microstructure of laser surface melted AISI 316L stainless steel with process parameters

88.46 W/mm² applied power density. On the other hand, the variation in thickness of columnar grains does not follow any specific trend with applied power density. However, it decreases with an increase in scan speed. The dendritic zone width, on the other hand, is found to increase with the increase in applied power density and decrease with an increase in scan speed. The morphological changes in the microstructure from columnar to dendritic and subsequently to equiaxed are due to higher local undercooling that occurred at the interface as compared to the same, which is required for nucleation resulting in blocking of columnar grains by dendrites or equiaxed grains grown in the undercooled region. The blocking mechanism may be mechanical, thermal, or solutal blocking, which was experienced earlier by several authors (Ref 49-51).

Figure 6(a) and (b) shows the XRD profiles after various LSM routines. While the microstructure remains the same austenitic with no new peak or phase, the individual peaks undergo a change in width due to accumulated lattice strain introduced by rapid cooling of LSM. This lattice strain was calculated using the Scherer formula: $L = k\lambda/(\beta \cos\theta)$ (whereas λ is the x-ray wavelength (Cu K- α), θ the diffraction angle, k is a constant shape factor (0.9), and β is the breadth at half-peak-height) and presented in Fig. 7.

In addition to strain, dislocation density associated with this strain was also calculated from the width of the XRD peaks and presented in Fig. 7. It is evident from Fig. 7 that both lattice strain and dislocation density increase with increase in P but marginally decrease with increase in v . It appears that the effect of power density is more prominent than scan speed in generating lattice strain. The existence of point and line defects caused by rapid quenching associated with LSM may be attributed to the lattice strain, which was also reported by Kumar et al. (Ref 38).

The residual stress introduced during LSM was measured by XRD using a dedicated goniometer. Figure 8(a) and (b) shows the residual stress variation with P and v and reveals that the residual stress increases with power density increase and

decreases scan speed increase. The residual stress is mostly tensile in nature, which is obviously due to the rapid solidification and contraction occurring during the ultrafast cooling cycle or self-quenching associated with LSM. Thus, this residual stress is proportional to the thermal gradient and rate of cooling experienced by the melt pool. When P rises, so does the temperature gradient and the rate of cooling, leading to a greater degree of residual stress. Also, when scan speed increases, the residual stress reduces since both the temperature gradient and rate of cooling decrease (Ref 52). It may be observed that the residual stress generated by LSM has a smaller magnitude than the yield strength of AISI 316L stainless steel (205 MPa). Hence, the introduced residual stress may reduce the load-bearing capacity of the specimen; however, it would not cause any damage on the surface.

Microhardness is a measure of the surface mechanical properties. Microhardness variation with vertical depth from the surface after LSM is shown in Fig. 9, along with various combinations of P and v (constant) and v and P (constant), demonstrating that LSM results in a significant increase in microhardness (260-336 VHN) compared to that of the as-received stainless steel (180 VHN). Besides that, the maximum microhardness found near the surface diminishes with increase in distance from the surface. This trend is usual, as reported by Kumar et al. (Ref 38), where the maximum reported microhardness was 375 VHN obtained after a similar LSM experiment. The effect of P and v on microhardness seems to follow opposite trend as the peak and average microhardness increases (260 to 336 VHN) with increase in P (58.98-88.46 W/mm²) but decreases (336 to 180 VHN) with increase in v , respectively. The variation in microhardness with power density is attributable to the reduction in average equiaxed grain size resulting from a faster cooling rate at higher P . Similarly, a higher scan speed results in a reduced microhardness of the melt zone as a result of a lower cooling rate at lower v . The same logic is attributed to decrease in microhardness with increase in vertical depth as the maximum temperature

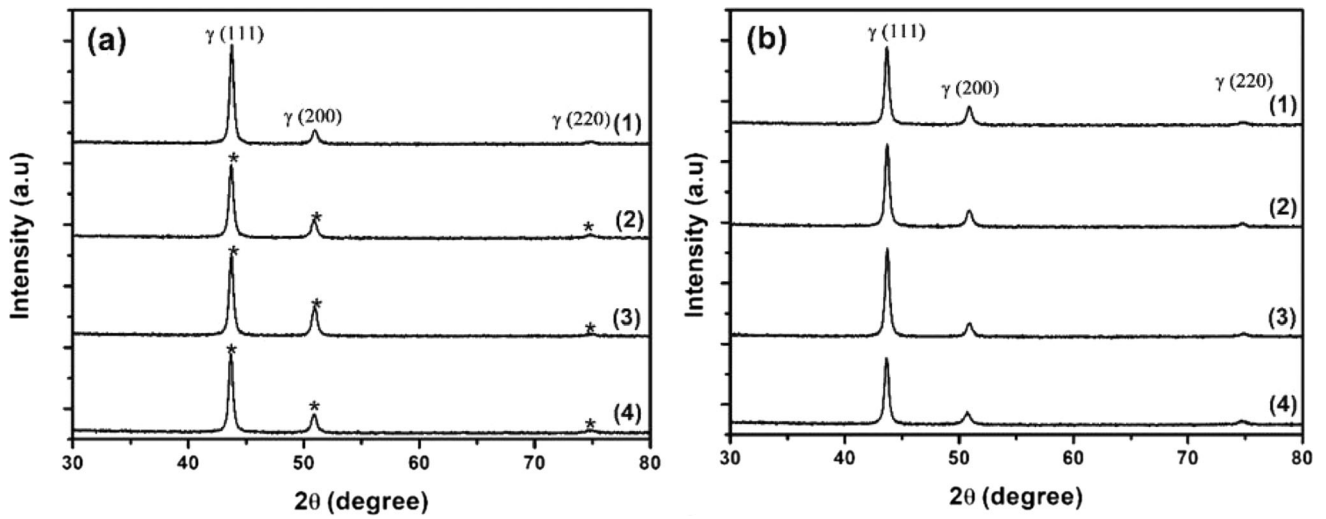


Fig 6 XRD profiles of AISI 316L stainless steel following LSM with (a) $P = 58.98 \text{ W/mm}^2$ (plot 1), 68.81 W/mm^2 (plot 2), 78.63 W/mm^2 (plot 3), and 88.46 W/mm^2 (plot 4) at $v = 20 \text{ mm/s}$ (constant), and (b) $v = 20 \text{ mm/s}$ (plot 1), 40 mm/s (plot 2), 60 mm/s (plot 3), and 80 mm/s (plot 4) at $P = 88.46 \text{ W/mm}^2$ (constant) respectively

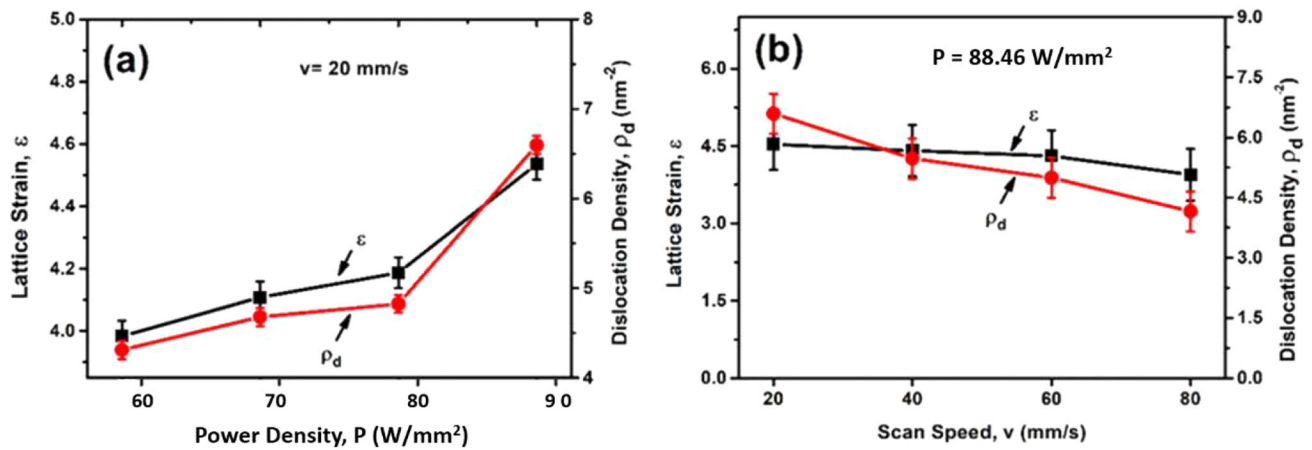


Fig 7 Variation of lattice strain (and dislocation density of following LSM with (a) $P = 58.98\text{-}88.46 \text{ W/mm}^2$ at $v = 20 \text{ mm/s}$, and (b) $v = 20\text{-}80 \text{ mm/s}$ at $P = 88.46 \text{ W/mm}^2$, respectively

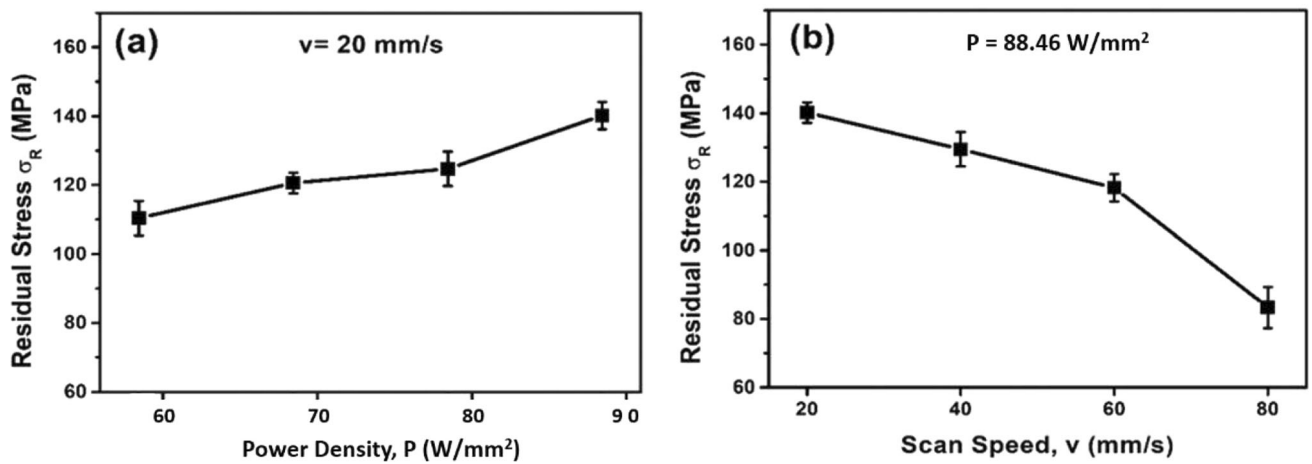


Fig. 8 Variation of residual stress following LSM with (a) $P = 58.98\text{-}88.46 \text{ W/mm}^2$ at $v = 20 \text{ mm/s}$, and (b) $v = 20\text{-}80 \text{ mm/s}$ at $P = 88.46 \text{ W/mm}^2$, respectively.

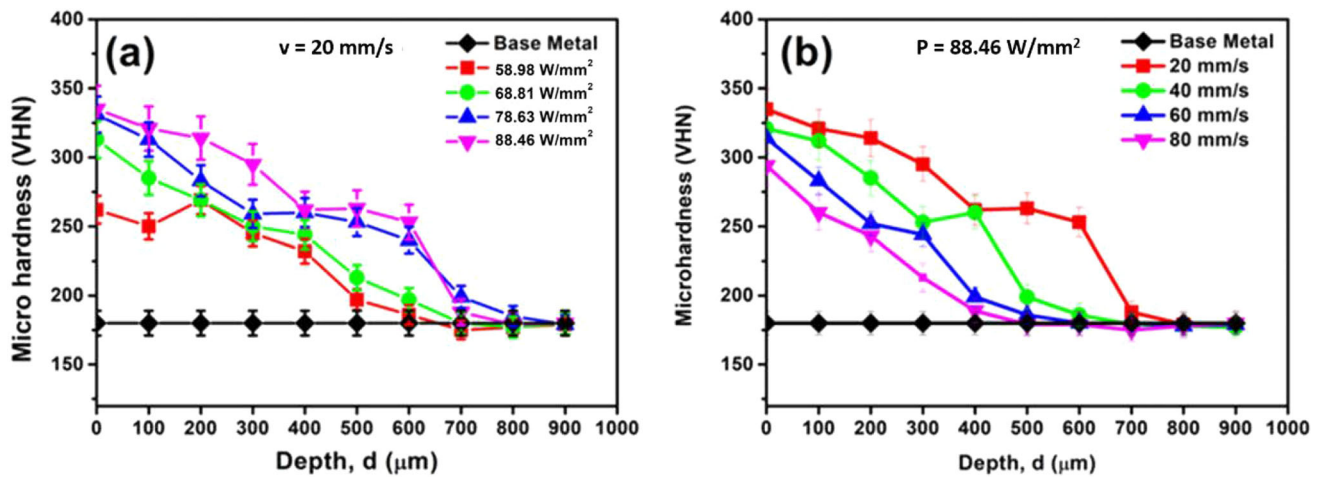


Fig. 9 Average microhardness with variation of vertical depth from the surface in as-received condition (for reference) and after LSM with (a) various levels of P at $v = 20$ mm/s, and (b) different levels of v at $P = 88.46$ W/mm², respectively

coincides with the top surface and minimum with the final depth of melting in a given cycle of LSM. As neither change in composition nor any phase transformation (other than melting and solidification) is expected in LSM of austenitic stainless steel, it may be concluded that refinement of microstructure or austenitic grain size is the main mechanism of enhancement of microhardness.

Figure 10(a), (b), (c), and (d) shows the nano-indentation behavior of AISI 316L stainless steel in as-received and after LSM in terms of the effect of power density (Fig. 10a, b) and scan speed (Fig. 10c, d), respectively, while LSM consistently improves nano-hardness than the as-received surface. With an increase in power density and a reduction in scan speed, these changes to the laser parameters helped to raise the nano-hardness. Two other relevant nano-mechanical properties derived from the nano-indentation curves, namely, elastic modulus and energy absorbed in the elastic regime (resilience), also show systematic variation though not very significantly, such that elastic modulus is proportional to power density but inversely related to scan speed, and resilience is proportional to scan speed but inversely related to power density (within the error limit). Nano-mechanical properties at low load (20 mN) are useful to determine the mechanical behavior of the near-surface region following LSM or similar surface engineering operations. It may be noted that the literature does not include any reports of such thorough nano-mechanical property evaluation of stainless steel after LSM.

Figure 11(a) and (b) shows the variation of the average surface roughness with P (at a constant $v = 20$ mm/s) and (b) v (at a constant $P = 88.46$ W/mm²). Average surface roughness developed after LSM increases with P but decreases with v under comparable conditions. In the past, similar behavior of variation of surface roughness with P was reported by Kumar et al. (Ref 38) following LSM of the same steel with a Nd:YAG laser. Increased surface roughness with increase in P is attributed to an increase in thermal gradient, causing surface tension assisted fluid flow during melting and, hence, ripple formation. Following a similar logic, the surface roughness increases with decrease in v .

Figure 12(a), (b), (c), (d), (e), and (f) shows the wear behavior of as-received specimen and subsequent to LSM against a sintered WC ball ($D = 10$ mm) under oscillating

fretting wear mode showing the variation of (a, c) coefficient of friction (COF), (b, d) cumulative depth of wear with time, and (e, f) specific wear rate showing the effects of P (Fig. 12a, c, e) and v (Fig. 12b, d, f) on wear behavior. It appears that COF initially increases linearly with a smooth/sharp increase in its magnitude with time, following which it remains almost steady, oscillating around a mean value during the steady state of wear till the end of the experiment. A comparison of the COF of samples in as-received condition and after LSM suggests that the COF of samples after LSM is marginally lower than that of as-received samples. A comparison of the COF of all samples shows that the COF is the minimum after LSM with $P = 88.46$ W/mm² at $v = 20$ mm/s (Fig. 12a, c). Similarly, Fig. 12(b) and (d) shows that wear depth or wear rate initially follows linear kinetics for a very short period of time, following which the rate remains almost steady thereafter. The detailed comparison of the wear behavior of samples after LSM with that of the as-received one reveals that the wear rate of LSM significantly reduces the wear and damage in stainless steel in all combinations of P and v . In this respect, the effect of P seems more prominent than that of v . This set of wear results are commensurate with the fact that LSM increases the hardness of stainless steel significantly (Fig. 9a). The same argument is valid for the reduction of COF and wear rate and volume with a decrease in v due to a concomitant increase in hardness with a decrease in v (Fig. 9b).

This study on the effect of LSM on the wear and tribology of austenitic stainless steel clearly establishes that LSM is quite effective in improving hardness and wear resistance without any compositional or microstructural intervention to the bulk. Moreover, the effect of P is more pronounced than v in enhancing wear resistance under comparable conditions, with the maximum improvement obtained at $P = 88.46$ W/mm² and $v = 20$ mm/s (Fig. 12e, f).

Scars on the wear tracks reveal important details about the mechanism of wear damage. Figure 13(a), (b), (c), (d), (e), and (f) shows the microstructures of the worn surface of (a, b) as-received specimen, (c, d) reveal the same after LSM with $P = 58.98$ W/mm² and $v = 20$ mm/s, and (e, f) present the same after LSM with $P = 88.46$ W/mm² and $v = 20$ mm/s, respectively. Comparison between Fig. 13(a), (c), and (e) clearly establishes that the extent and severity of wear damage

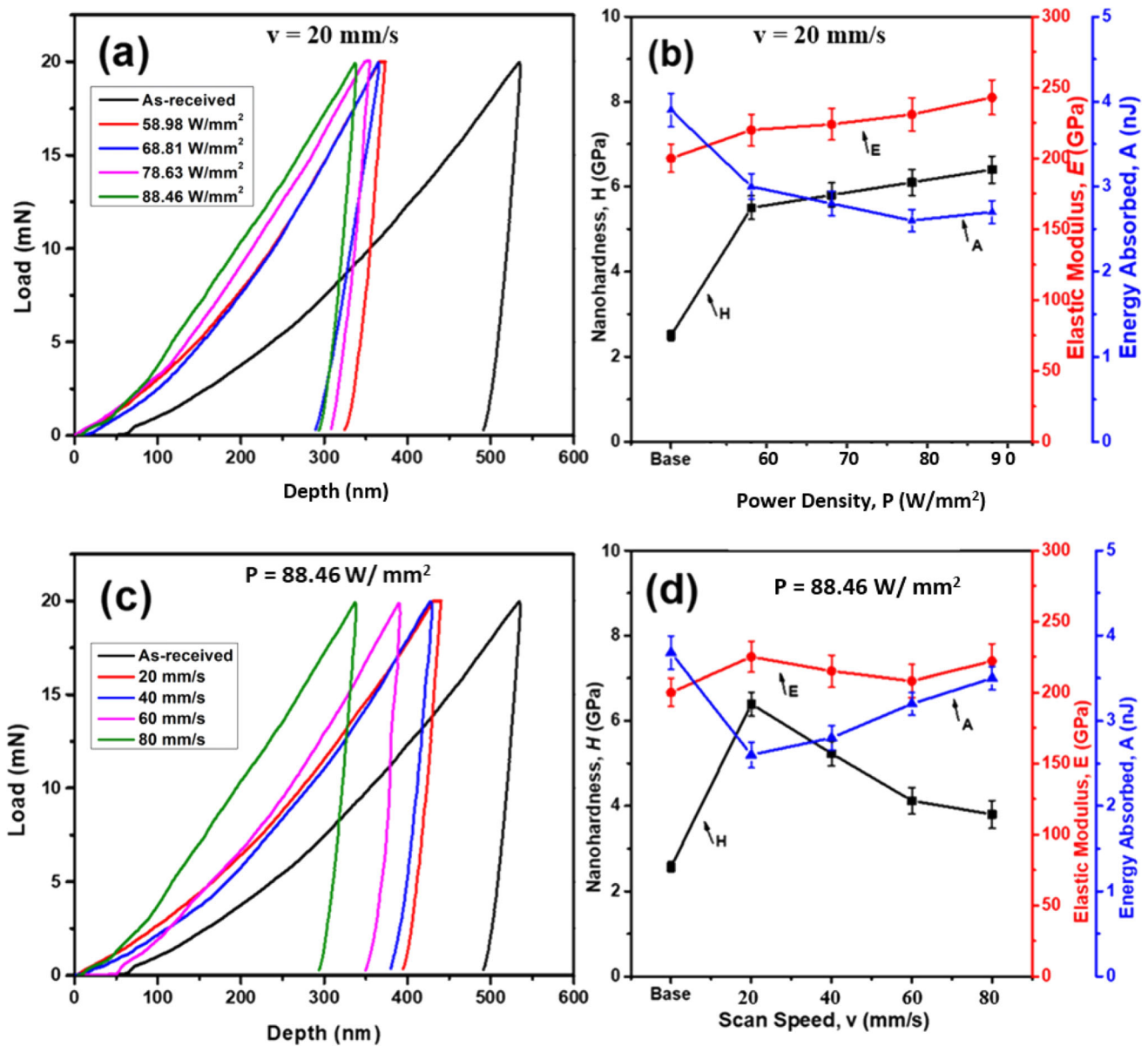


Fig. 10 Surface mechanical properties at 20 mN of load obtained by nano-indentation studies of samples subjected to LSM with (a) varying $P = 58.98\text{--}88.46 \text{ W/mm}^2$ at $v = 20 \text{ mm/s}$ with corresponding summary of the (b) variation of nano-hardness, elastic modulus and energy absorbed with P ; and the same for (c) variation of $v = 20\text{--}80 \text{ mm/s}$ at $P = 88.46 \text{ W/mm}^2$ with (d) summary of the same set of nano-mechanical properties as a function of v

is significantly reduced after LSM than that in as-received stainless steel. The high magnification views in Fig. 13(b), (d), and (f) in comparison with their low magnification images in Fig. 13(a), (c), and (e) reveal that the worn surface of as-received steel consists of loose worn debris along with the presence of microcracks. In contrast, the size and volume of such debris are considerably smaller and lower, with smaller density of microcracks in the worn surfaces in samples after LSM. In addition, small areas of fretting-assisted micro-deformation band are noticed in worn tracks in samples after LSM. A close examination suggests that worn surfaces of as-received stainless steel contain some micro-holes and micro-pits (Fig. 13a). As a result of this extensive examination of the worn surfaces, it is possible to infer that the process of wear in all instances includes the combined action of fretting and abrasive wear. While the formation of debris is primarily due to

abrasive wear, as revealed by the fine micro-scratches mostly covered by the worn debris and damage on the surface, wear in both as-received condition and after LSM is mostly contributed by the effect of both high-stress abrasion and fretting wear. The extent of damage, as already pointed out, is significantly lower in samples after LSM, mainly due to the higher hardness and related mechanical properties (higher elastic modulus and lower COF) of the samples compared to that of as-received AISI 316L stainless steel.

A detailed study of the corrosion behavior of AISI 316L stainless steel samples in as-received condition and after LSM was carried out in 3.56 wt.% NaCl solution by potentiodynamic polarization test to determine the relevant corrosion resistance parameters like corrosion potential (E_{corr}), the critical potential for pit formation (E_{pit}), and corrosion rate, as depicted in Fig. 14(a) and (b) and summarized in Table 2. From Table 2, it

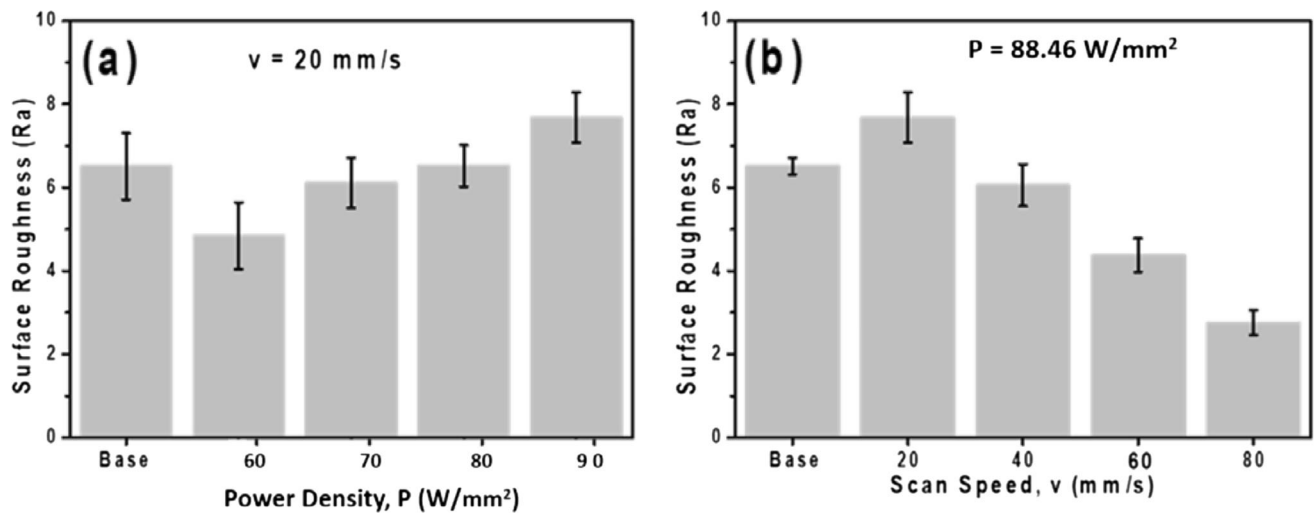


Fig. 11 Variation of surface roughness with (a) P at a constant $v = 20 \text{ mm/s}$ and (b) v at a constant $P = 88.46 \text{ W}/\text{mm}^2$, respectively

is observed that E_{corr} of the as-received AISI 316L stainless steel is -0.42 V (Ag/AgCl), which is in tune with the similar result (-0.43 V , Ag/AgCl) reported by Savaloni et al. (Ref 53). The studies were conducted either with varying P at $v = 20 \text{ mm/s}$ or with varying v at $P = 88.46 \text{ W}/\text{mm}^2$. Figure 14(a) and (b) and Table 2 suggest that the corrosion rate decreases and the corrosion potential shifts toward the noble direction as the power density increases. In addition, the E_{pit} also shifts toward the noble direction. The improvement in corrosion resistance with increase in laser power density is mainly due to the increased degree of microstructural refinement and homogenization with increase in applied power density. On the other hand, by increasing the scan speed, there is deterioration of pitting corrosion resistance, in terms of shifting of E_{pit} toward active direction. Furthermore, there is increase in corrosion rate as a signature of decreased corrosion resistance with increase in scan speed. Deterioration in corrosion resistance property with an increase in scan speed is attributed to the coarsening of microstructure and an increase in segregation with an increase in scan speed. A careful study of the corrosion rate shown in Fig. 14(a) and (b) and Table 2 reveal that LSM accounts for nearly two orders of magnitude decrease in corrosion rate as compared to that in as-received stainless steel specimens. This decrease in corrosion rate caused by LSM might be directly related to microstructural refinement and compositional homogeneity, as has previously been reported and established in various other alloy systems (Ref 54, 55). A careful investigation of the variation of the corrosion rate with v reveals that the corrosion rate is lowest after LSM with $P = 88.46 \text{ W}/\text{mm}^2$ and $v = 20 \text{ mm/s}$. A similar careful analysis of the values of critical potential for pit formation reveals that E_{pit} shifts toward a nobler direction except for the sample processed with $P = 58.98 \text{ W}/\text{mm}^2$ and $v = 20 \text{ mm/s}$. A similar range of E_{pit} values was observed by Kumar et al. (Ref 38) in as-received ($E_{\text{pit}} = -0.319 \text{ V}$) and laser surface melted AISI 316L stainless steel (E_{pit} ranges from -0.07 to 0.158 V). To understand the corrosion behavior and mechanism of corrosion resistance, electron backscatter diffraction (EBSD) analysis was performed on the microstructure, as described below.

Figure 15(a) and (b) reveals the significant degree of grain size reduction caused by LSM as compared to that in as-

received stainless steel. Comparison between Fig. 15(a) and (b) demonstrates that the area fraction of high-angle grain boundaries in as-received steel is more than double (0.578) than that produced by LSM (0.215). In contrast, the area fraction of low-angle grain boundaries is much higher after LSM (0.101) as compared to that in as-received steel (0.062). The presence of a greater percentage of high-angle grain boundaries in the as-received AISI 316L stainless steel results in an increased corrosion rate. Also, due to higher area fraction of the low-angle grain boundaries (LAGB) produced by LSM, protective oxide film forms uniformly throughout the surface. The potential differences among the grains may increase due to low LAGB by an increase in temperature after LSM (Ref 56). In addition, the oxide film is more stable and stronger because of a larger fraction of LAGB after LSM as compared to that in as-received specimen.

Figure 16(a) and (b) compares the KAM misorientation maps of the present stainless steel in as-received condition with that after LSM and reveal that due to LSM, the magnitude of strain is reduced, and it is uniformly distributed. On the other hand, the strain mapping is not uniform in the as-received AISI 316L stainless steel, as isolated regions of high strain are seen discontinuously distributed throughout the surface. Due to the presence of a highly strain region in the microstructure, the probability of localized damage and the formation of pits is more in as-received sample. In addition, these localized strain pockets are likely to form wider numbers of micro-galvanic cells in various parts of the microstructure, increasing more chances of galvanic corrosion damage and pit formation in as-received steel than that of laser surface melted AISI 316L stainless steel (Ref 57).

Figure 17(a) and (b) clearly shows that the same steel before and after LSM develops vastly different orientation distribution with much smaller and more randomly distributed regions or crystallites of contrasting orientations separated by high-angle boundaries of large curvature in as-received condition (Fig. 17a), which changes to significantly large areas of regions of multiple grains or crystallites of nearly identical orientation as if a large region of the microstructure after LSM bear the same orientation (or negligible misorientation) drastically reducing the scope of galvanic action over a large area. More precisely, LSM drastically reduces the area fraction of orien-

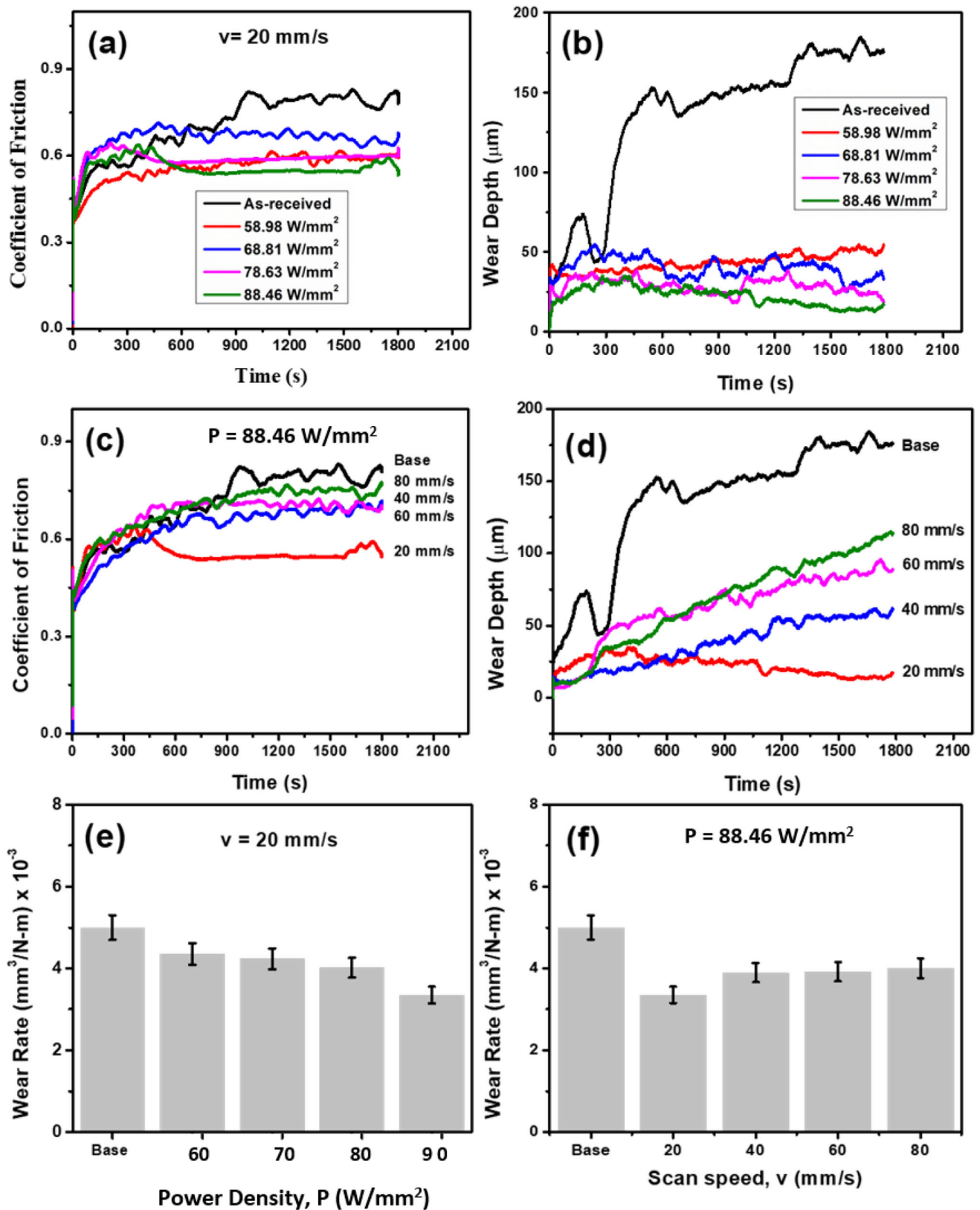


Fig. 12 Variation of wear behavior in terms of (a, c) coefficient of friction, (b, d) cumulative depth of wear and wear rate as a function of (e) P (with $v = 20$ mm/s) and (f) v (with $P = 88.46$ W/mm²)

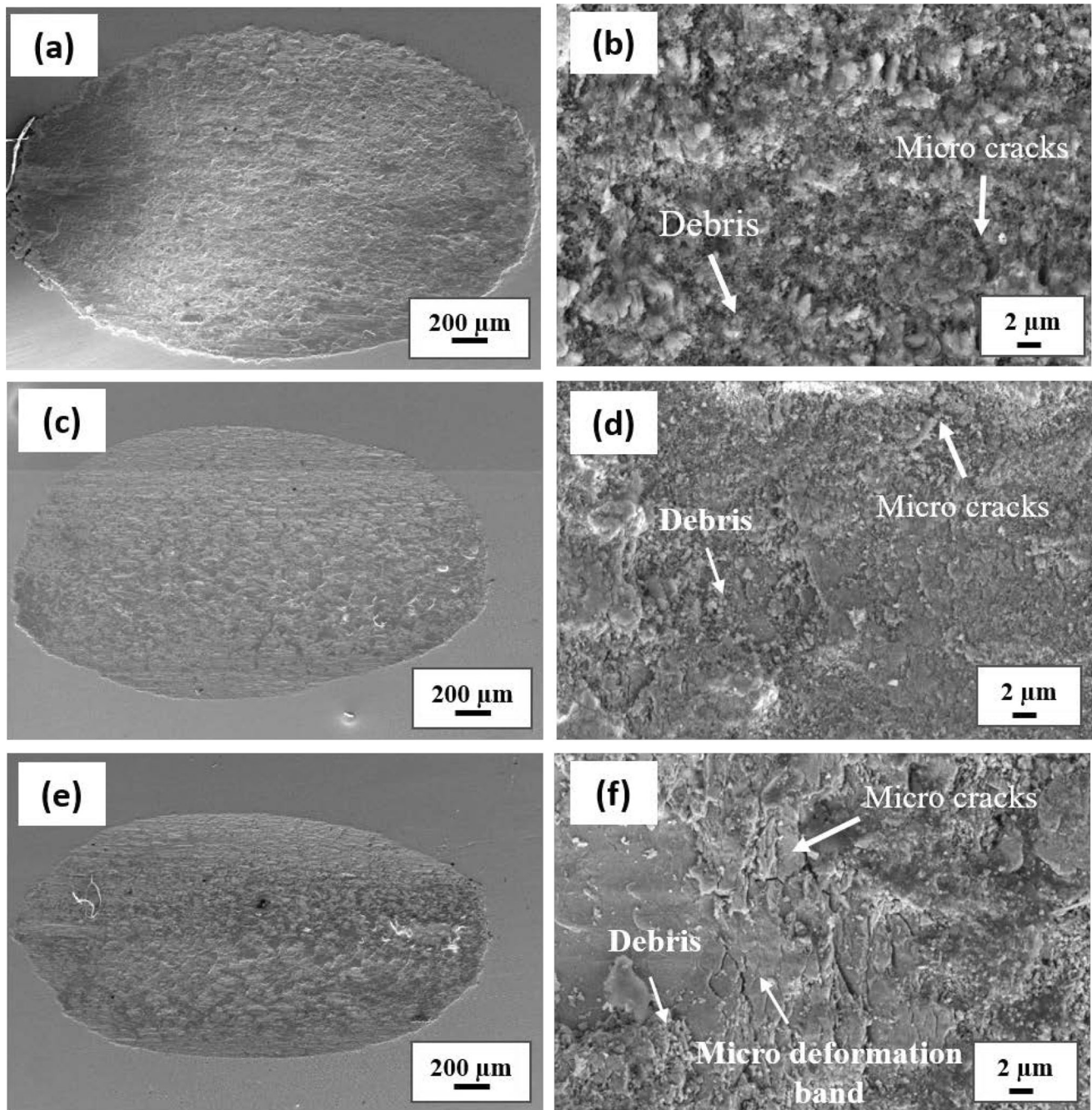


Fig. 13 SEM images of worn scars of (a, b) as-received steel and the same after LSM with (c, d) $P = 58.98 \text{ W/mm}^2$ and $v = 20 \text{ mm/s}$, and (e, f) $P = 88.46 \text{ W/mm}^2$ and $v = 20 \text{ mm/s}$, respectively. Note that Figs. b, d, and f are the high magnification view of a, c, e, respectively

tation mismatch compared to the same steel prior to LSM. This difference in microstructure and orientation distribution is a big reason why AISI 316L stainless steel after LSM has less chemical reactivity and better corrosion resistance properties than that in the as-received condition.

4. Summary and Conclusions

In the current investigation, microhardness, wear resistance, and corrosion resistance properties of AISI 316L stainless steel have been carefully measured and compared between samples

prior to and following LSM (with $P = 58.98\text{-}88.46 \text{ W/mm}^2$ and $v = 20\text{-}80 \text{ mm/s}$). Detailed analysis of the results indicates:

- The lattice strain, dislocation density, and residual stress after LSM rise with applied power density (from 58.98 to 88.46 W/mm^2) and decrease with an increase in scan speed (from 20 to 80 mm/s).
- The microstructure and phase prior to and after LSM remain identical, i.e., single-phase austenitic with no new phase evolving or precipitating due to LSM.
- According to SEM analysis, LSM causes a significant amount of grain refinement in comparison with that of the as-received steel (from 40-50 μm to 1-2 μm).

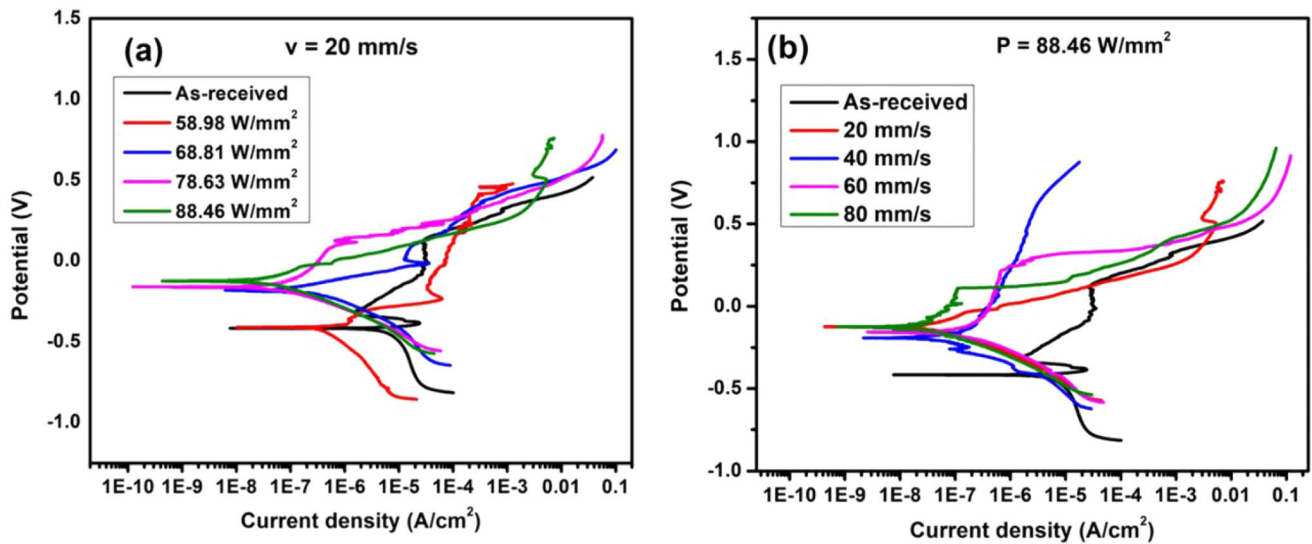


Fig. 14 Potentiodynamic corrosion plots in terms of variation of potential with current density AISI 316L stainless steel samples in as-received condition and after LSM showing the effect of (a) P (at $v = 20$ mm/s) and (b) v (at $P = 88.46$ W/mm²), respectively

Table 2 Summary of results of potentiodynamic polarization tests

Power density, W/mm ²	Scan speed, mm/s	E_{corr} , V	I_{corr} , A/cm ²	Corrosion rate, mm/year $\times 10^{-3}$	E_{pit} , V
	As-received AISI 316L stainless steel	-0.42 ± 0.021	$4.43^{-5} \pm 0.2215$	461.00 ± 23.05	-0.32 ± 0.016
58.98	20	-0.41 ± 0.0205	$6.38^{-7} \pm 0.319$	6.66 ± 0.33	-0.36 ± 0.018
68.81	20	-0.19 ± 0.0095	$2.14^{-7} \pm 0.107$	2.24 ± 0.112	0.01 ± 0.0005
78.63	20	-0.16 ± 0.008	$1.38^{-7} \pm 0.069$	1.44 ± 0.072	0.13 ± 0.0065
88.46	20	-0.12 ± 0.006	$4.73^{-8} \pm 0.2365$	0.49 ± 0.025	0.54 ± 0.027
88.46	40	-0.24 ± 0.012	$1.28^{-7} \pm 0.064$	1.30 ± 0.065	0.42 ± 0.021
88.46	60	-0.16 ± 0.008	$1.29^{-7} \pm 0.065$	1.35 ± 0.067	0.22 ± 0.011
88.46	80	-0.13 ± 0.0065	$1.51^{-7} \pm 0.059$	1.54 ± 0.062	0.11 ± 0.0055

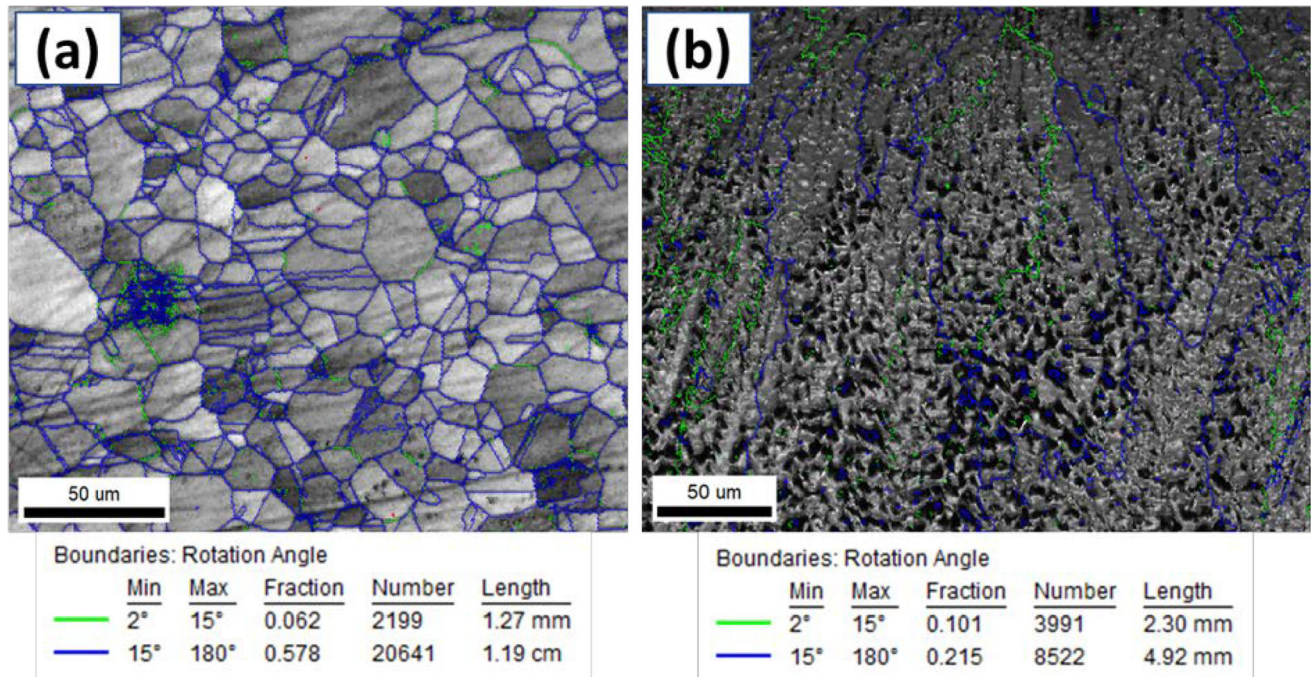


Fig. 15 EBSD images showing grain boundary distribution of AISI 316L stainless steel (a) in as-received condition and (b) after LSM with $P = 88.46$ W/mm² and $v = 20$ mm/s

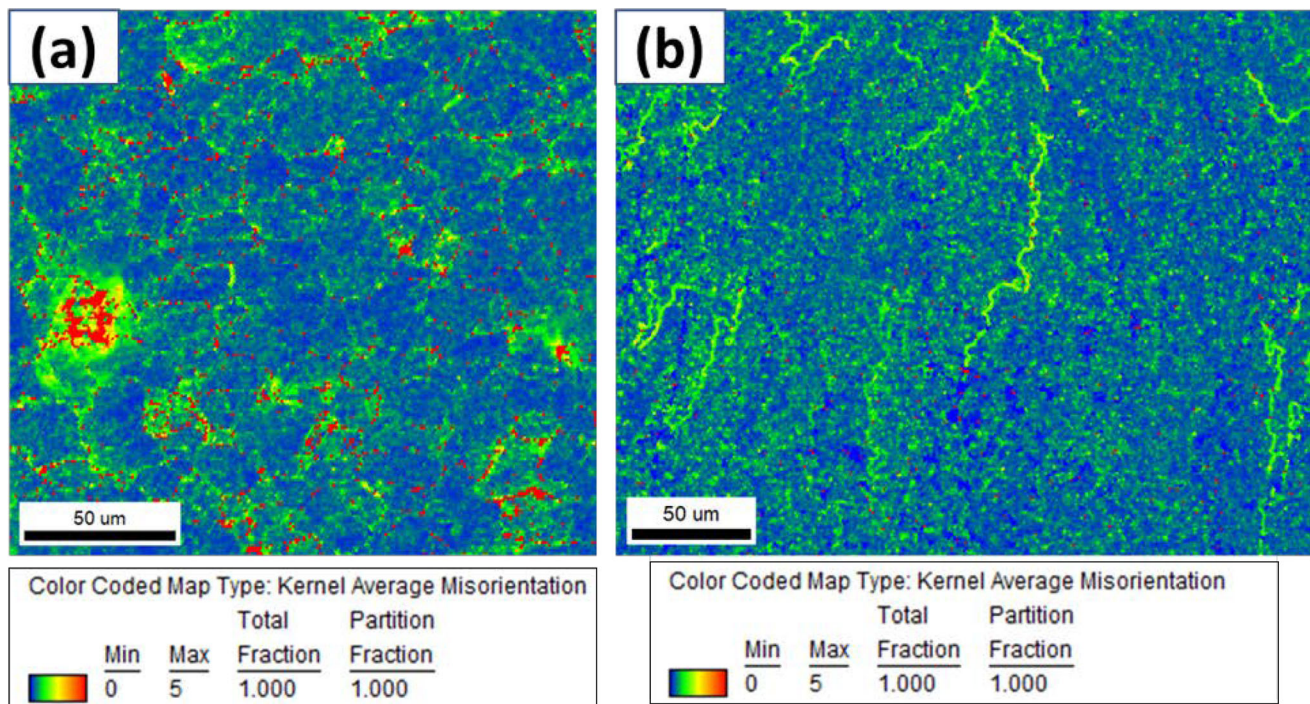


Fig. 16 Misorientation (KAM) mapping of AISI 316L stainless steel in (a) as-received condition, and (b) after LSM with $P = 88.46 \text{ W/mm}^2$ and $v = 20 \text{ mm/s}$

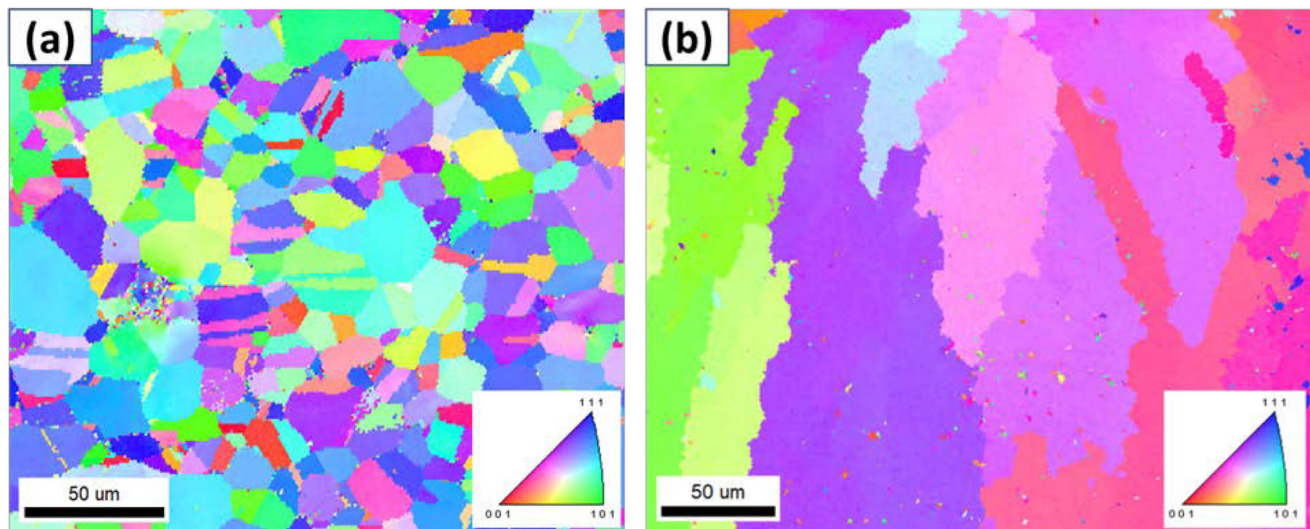


Fig. 17 Inverse pole figure (IPF) mapping of AISI 316L stainless steel in (a) as-received condition and (b) after LSM with $P = 88.46 \text{ W/mm}^2$ and $v = 20 \text{ mm/s}$

- Due to this considerable grain refinement, average microhardness after LSM is significantly enhanced (180-336 VHN) as compared to that (155 VHN) of as-received specimen.
- Both wear rate and cumulative wear volume are much lower in samples after LSM than that in the as-received condition. Moreover, the wear rate and wear volume both drop when laser power density is increased (from 58.98 to 88.46 W/mm^2); however, they rise as scan speed is increased (from 20 to 80 mm/s). LSM at $P = 88.46 \text{ W/mm}^2$ and $v = 20 \text{ mm/s}$ offers the highest improvement in wear resistance.
- Samples after LSM show a sharp increase in the coefficient of friction only at the beginning of dry sliding wear, which subsequently reduces and remains nearly constant thereafter. In fact, worn surfaces of samples after LSM are discontinuous in nature with the evidence of micro-roughening due to the accumulation of worn debris and its adherence to the surface.
- LSM induces enhanced corrosion resistance than that of as-received AISI 316L stainless steel, particularly after LSM with $P = 88.46 \text{ W/mm}^2$ and $v = 20 \text{ mm/s}$.

- The improved corrosion resistance under optimum conditions is attributed to (a) microstructure refinement and homogenization, (b) increased area fraction of low-angle grain boundaries and decreased area fraction of high-angle grain boundaries promoting formation of stable and stronger passive film, (c) homogeneous and reduced strain distribution as confirmed by KAM mapping, and (d) reduced area fraction of orientation mismatch between grains.

Acknowledgments

I.M. would like to acknowledge partial financial support from DST sponsored Projects 'JCP' (SR/S2/JCB-16/2012. Dt.16-10-2017) and 'DGL' (DST/TSG/AMT/2015/636/G, Dt.18-06-2018), ISRO sponsored Project 'ONC' (IIT/KCSTC/CHAIR/NEW/P/18-19/01, Dt.24-05-2018), Ministry of Education sponsored Project 'LSL_SKI' (SPARC/2018-2019/P723/SL, Dt.31-05-2019), Science and Engineering Research Board, N. Delhi (POWER Fellowship, SPF/2021/000073, Dt. 11-03-2021) and Ministry of Human Resource Development (MHRD), Government of India (under IMPRINT-2, sanction letter IMP/2018/001162, Dt. 02-01-2019).

References

- U.I. Thomann and P.J. Uggowitzer, Wear-Corrosion Behavior of Biocompatible Austenitic Stainless Steels, *Wear*, 2000, **239**(1), p 48–58.
- D. Kuroda, S. Hiromoto, T. Hanawa, and Y. Katada, Corrosion Behavior of Nickel-Free High Nitrogen Austenitic Stainless Steel in Simulated Biological Environments, *Mater. Trans.*, 2002, **43**(12), p 3100–3104.
- M.G. Fontana, N.D. Greene, and J. Klerer, Corrosion Engineering, *J. Electrochem. Soc.*, 1968, **115**(5), p 142C. <https://doi.org/10.1149/1.2411256>
- K.G. Budinski, *Surface Engineering for Wear Resistance (Retroactive Coverage)*, Prentice-Hall, Inc, Englewood Cliffs, 1988, p 420
- J. Dutta Majumdar and I. Manna, Laser Material Processing, *Int. Mater. Rev.*, 2011, **56**(5–6), p 341–388.
- S. Jannat, H. Rashtchi, M. Atapour, M.A. Golozar, H. Elmkhah, and M. Zhiani, Preparation and Performance of Nanometric Ti/TiN Multi-Layer Physical Vapor Deposited Coating on 316L Stainless Steel as Bipolar Plate for Proton Exchange Membrane Fuel Cells, *J. Power Sources*, 2019, **435**, p 226818.
- T. Rajabi, M. Atapour, H. Elmkhah, and S.M. Nahvi, Nanometric CrN/CrAlN and CrN/ZrN Multilayer Physical Vapor Deposited Coatings on 316L Stainless Steel as Bipolar Plate for Proton Exchange Membrane Fuel Cells, *Thin Solid Films*, 2022, **753**, p 139288.
- N. Ali, J.A. Teixeira, A. Addali, M. Saeed, F. Al-Zubi, A. Sedaghat, and H. Bahzad, Supplementary Materials: Deposition of Stainless Steel Thin Films: An Electron Beam Physical Vapour Deposition Approach, *Materials (Basel)*, 2019, **12**, p 571. <https://doi.org/10.3390/ma12040571>
- W. Zhu, Z. Su, J. Guo, K. Li, K. Chen, W. Li, A. Yi, Z. Liao, Y. Luo, Y. Hu, Y. Xu, Q. Lin, and X. Meng, Preparation and Characterization of Diamond-like Carbon (DLC) Film on 316L Stainless Steel by Microwave Plasma Chemical Vapor Deposition (MPCVD), *Diam. Relat. Mater.*, 2022, **122**, p 108820.
- M. Sabzi, S.H. Mousavi Anijdan, and M. Asadian, The Effect of Substrate Temperature on Microstructural Evolution and Hardenability of Tungsten Carbide Coating in Hot Filament Chemical Vapor Deposition, *Int. J. Appl. Ceram. Technol.*, 2018, **15**(6), p 1350–1357. <https://doi.org/10.1111/IJAC.12905>
- M.H. Staia, B. Lewis, J. Cawley, and T. Hudson, Chemical Vapour Deposition of TiN on Stainless Steel, *Surf. Coat. Technol.*, 1995, **76–77**, p 231–236.
- E. García, J.F. Louvier-Hernández, G. Mendoza-Leal, M. Flores-Martínez and C. Hernández-Navarro, Tribological Study of HAp/CTS Coatings Produced by Electrodeposition Process on 316L Stainless Steel, *Mater. Lett.*, 2020, **277**, p 128336.
- L. Xu, Y. Zuo, J. Tang, Y. Tang, and P. Ju, Chromium-Palladium Films on 316L Stainless Steel by Pulse Electrodeposition and Their Corrosion Resistance in Hot Sulfuric Acid Solutions, *Corros. Sci.*, 2011, **53**(11), p 3788–3795.
- F. Laroudie, C. Tassin, and M. Pons, Hardening of 316L Stainless Steel by Laser Surface Alloying, *J. Mater. Sci.*, 1995, **30**(14), p 3652–3657. <https://doi.org/10.1007/BF00351880/METRICS>
- E.S. Ghaith, S. Hodgson, and M. Sharp, Laser Surface Alloying of 316L Stainless Steel Coated with a Bioactive Hydroxyapatite-Titanium Oxide Composite, *J. Mater. Sci. Mater. Med.*, 2015, **26**(2), p 1–8. <https://doi.org/10.1007/S10856-015-5399-1/FIGURES/8>
- J. Dutta Majumdar, A. Weisheit, B.L. Mordike, and I. Manna, Laser Surface Alloying of Ti with Si, Al and Si+Al for an Improved Oxidation Resistance, *Mater. Sci. Eng. A*, 1999, **266**(1–2), p 123–134.
- M. Cabeza, G. Castro, P. Merino, G. Pena, and M. Román, Laser Surface Melting: A Suitable Technique to Repair Damaged Surfaces Made in 14 Ni (200 Grade) Maraging Steel, *Surf. Coatings Technol.*, 2012, **212**, p 159–168.
- N.B. Dahotre, Laser Material Processing by W.M. Steen Springer-Verlag, London, England 206 Pages, Soft Cover, 1991, *Mater. Manuf. Process.*, 1993, **8**(3), p 399–400. <https://doi.org/10.1080/10426919308934845>
- J. Dutta Majumdar, R. Galun, B.L. Mordike, and I. Manna, Effect of Laser Surface Melting on Corrosion and Wear Resistance of a Commercial Magnesium Alloy, *Mater. Sci. Eng. A*, 2003, **361**, p 119–129. [https://doi.org/10.1016/S0921-5093\(03\)00519-7](https://doi.org/10.1016/S0921-5093(03)00519-7)
- J. Dutta Majumdar, A.K. Nath, and I. Manna, Studies on Laser Surface Melting of Tool Steel—Part II: Mechanical Properties of the Surface, *Surf. Coatings Technol.*, 2010, **204**(9–10), p 1326–1329. <https://doi.org/10.1016/j.surfcoat.2009.08.012>
- C.T. Kwok, H.C. Man, and F.T. Cheng, Laser Surface Melting of Tool Steels H13, O1 and D6, in *26th International Congress on Applications of Lasers Electro-Optics, ICALOE 2007—Congress Proceedings*, vol. 523 (2007). <https://doi.org/10.2351/1.5061197>
- K.A. Qureshi, N. Hussain, J.I. Akhter, N. Khan, and A. Hussain, Surface Modification of Low Alloy Steel by Laser Melting, *Mater. Lett.*, 2005, **59**(6), p 719–722. <https://doi.org/10.1016/j.matlet.2004.08.040>
- M. Paczkowska, The Evaluation of the Influence of Laser Treatment Parameters on the Type of Thermal Effects in the Surface Layer Microstructure of Gray Irons, *Opt. Laser Technol.*, 2016, **76**, p 143–148. <https://doi.org/10.1016/j.optlastec.2015.07.016>
- M. Li, Y. Wang, B. Han, W. Zhao, and T. Han, Microstructure and Properties of High Chrome Steel Roller after Laser Surface Melting, *Appl. Surf. Sci.*, 2009, **255**(17), p 7574–7579. <https://doi.org/10.1016/j.apsusc.2009.04.030>
- C.T. Kwok, F.T. Cheng, and H.C. Man, Microstructure and Corrosion Behavior of Laser Surface-Melted High-Speed Steels, *Surf. Coatings Technol.*, 2007, **202**(2), p 336–348. <https://doi.org/10.1016/j.surfcoat.2007.05.085>
- Z. Liu, P.H. Chong, P. Skeldon, P.A. Hilton, J.T. Spencer, and B. Quayle, Fundamental Understanding of the Corrosion Performance of Laser-Melted Metallic Alloys, *Surf. Coatings Technol.*, 2006, **200**(18–19), p 5514–5525. <https://doi.org/10.1016/j.surfcoat.2005.07.108>
- Z. Liu, P.H. Chong, A.N. Butt, P. Skeldon, and G.E. Thompson, Corrosion Mechanism of Laser-Melted AA 2014 and AA 2024 Alloys, *Appl. Surf. Sci.*, 2005, **247**(1–4), p 294–299. <https://doi.org/10.1016/j.apsusc.2005.01.067>
- H.C. Man, Z.D. Cui, and T.M. Yue, Corrosion Properties of Laser Surface Melted NiTi Shape Memory Alloy, *Scr. Mater.*, 2001, **45**(12), p 1447–1453. [https://doi.org/10.1016/S1359-6462\(01\)01182-4](https://doi.org/10.1016/S1359-6462(01)01182-4)
- C.Y. Cui, Y.X. Shu, X.G. Cui, and J.D. Hu, Microstructure Evolution and Wear Behavior of AISI 304 Stainless Steel after Nd:YAG Pulsed Laser Surface Melting, *Appl. Opt.*, 2020, **59**(34), p 10862.
- S. Jafar, M. Kadhim, and S. Faayadh, Effect of Laser Surface Melting on Chromium Carbide of 304 Stainless Steels, *Eng. Technol. J.*, 2018, **36**(3A), p 344–349.
- A. Mahanti Ghosal, R.K. Gupta, K. Chandra, V. Bhardwaj, B.N. Upadhyaya, P. Ganesh, R. Kaul, and V. Kain, Laser Surface Melting of 304L SS: Increase in Resistance to Transpassive Dissolution and Pitting Corrosion, *Corros. Eng. Sci. Technol.*, 2023, **58**(5), p 508–520. <https://doi.org/10.1080/1478422X.2023.2212466>

32. O.V. Akgun and O.T. Inal, Laser Surface Melting and Alloying of Type 304 L Stainless Steel Part I Microstructural Characterization, *J. Mater. Sci.*, 1995, **30**, p 6097–6104.
33. N. Parvathavarthini, R.V. Subbarao, S. Kumar, R.K. Dayal, and H.S. Khatak, Elimination of Intergranular Corrosion Susceptibility of Cold-Worked and Sensitized AISI 316 SS by Laser Surface Melting, *J. Mater. Eng. Perform.*, 2001, **10**(1), p 5–13.
34. C.T. Kwok, H.C. Man, and F.T. Cheng, Cavitation Erosion and Pitting Corrosion of Laser Surface Melted Stainless Steels, *Surf. Coat. Technol.*, 1998, **99**(3), p 295–304.
35. J. Ghorbani, J. Li, and A.K. Srivastava, Application of Optimized Laser Surface Re-melting Process on Selective Laser Melted 316L Stainless Steel Inclined Parts, *J. Manuf. Process.*, 2020, **56**, p 726–734.
36. F. Vilchez, F. Pineda, M. Walczak, and J. Ramos-Grez, The Effect of Laser Surface Melting of Stainless Steel Grade AISI 316L Welded Joint on Its Corrosion Performance in Molten Solar Salt, *Sol. Energy Mater. Sol. Cells*, 2020, **213**(November 2019), p 110576. <https://doi.org/10.1016/j.solmat.2020.110576>
37. V.K. Balla, S. Dey, A.A. Muthuchamy, G.D. JanakiRam, M. Das, and A. Bandyopadhyay, Laser Surface Modification of 316L Stainless Steel, *J. Biomed. Mater. Res. Part B Appl. Biomater.*, 2018, **106**, p 569–577. <https://doi.org/10.1002/jbm.b.33872>
38. A. Kumar, S.K. Roy, S. Pityana, and J. Dutta Majumdar, Surface Characterization and Wear Behavior of Laser Surface Melted AISI 316L Stainless Steel, *Lasers Eng.*, 2012, **24**, p 147.
39. J.D. Majumdar, A. Kumar, S. Pityana, and I. Manna, Laser Surface Melting of AISI 316L Stainless Steel for Bio-Implant Application, *Proc. Natl. Acad. Sci. India Sect. A Phys. Sci.*, 2018, **88**(3), p 387–403. <https://doi.org/10.1007/S40010-018-0524-4/FIGURES/24>
40. C.T. Kwok, K.H. Lo, F.T. Cheng, and H.C. Man, Effect of Processing Conditions on the Corrosion Performance of Laser Surface-Melted AISI 440C Martensitic Stainless Steel, *Surf. Coat. Technol.*, 2003, **166**(2–3), p 221–230. [https://doi.org/10.1016/S0257-8972\(02\)00782-X](https://doi.org/10.1016/S0257-8972(02)00782-X)
41. C.T. Kwok, K.H. Lo, W.K. Chan, F.T. Cheng, and H.C. Man, Effect of Laser Surface Melting on Intergranular Corrosion Behaviour of Aged Austenitic and Duplex Stainless Steels, *Corros. Sci.*, 2011, **53**(4), p 1581–1591. <https://doi.org/10.1016/j.corsci.2011.01.048>
42. A. Ebrahimi, M. Sattari, A. Babu, A. Sood, G.W.R.B.E. Römer, and M.J.M. Hermans, Revealing the Effects of Laser Beam Shaping on Melt Pool Behaviour in Conduction-Mode Laser Melting, *J. Mater. Res. Technol.*, 2023, **27**(November), p 3955–3967. <https://doi.org/10.1016/j.jmrt.2023.11.046>
43. L. Han and F.W. Liou, Numerical Investigation of the Influence of Laser Beam Mode on Melt Pool, *Int. J. Heat Mass Transf.*, 2004, **47**(19–20), p 4385–4402.
44. A. Aggarwal, S. Patel, and A. Kumar, Selective Laser Melting of 316L Stainless Steel: Physics of Melting Mode Transition and Its Influence on Microstructural and Mechanical Behavior, *JOM Miner. Met. Mater. Soc.*, 2019, **71**(3), p 1105–1116. <https://doi.org/10.1007/S11837-018-3271-8/TABLES/2>
45. J. Wu, C. Zhang, P. Jiang, C. Li, H. Cao, and S. Shi, A Prediction Approach of Fiber Laser Surface Treatment Using Ensemble of Metamodels Considering Energy Consumption and Processing Quality, *Green Manuf. Open*, 2022, **1**(1), p 3. <https://doi.org/10.20517/GMO.2022.04>
46. S. Mishra, K. Narasimhan, and I. Samajdar, Deformation Twinning in AISI 316L Austenitic Stainless Steel: Role of Strain and Strain Path, *Mater. Sci. Technol.*, 2007, **23**(9), p 1118–1126. <https://doi.org/10.1179/174328407X213242>
47. C. Carboni, P. Peyre, G. Béranger, and C. Lemaitre, Influence of High Power Diode Laser Surface Melting on the Pitting Corrosion Resistance of Type 316L Stainless Steel, *J. Mater. Sci.*, 2002, **37**(17), p 3715–3723. <https://doi.org/10.1023/A:1016569527098/METRICS>
48. R.K. Rajan, S. Bontha, M.R. Ramesh, M. Das, and V.K. Balla, Laser Surface Melting of Mg-Zn-Dy Alloy for Better Wettability and Corrosion Resistance for Biodegradable Implant Applications, *Appl. Surf. Sci.*, 2019, **480**(18), p 70–82. <https://doi.org/10.1016/j.apsusc.2019.02.167>
49. J.D. Hunt, Steady State Columnar and Equiaxed Growth of Dendrites and Eutectic, *Mater. Sci. Eng.*, 1984, **65**(1), p 75–83. [https://doi.org/10.1016/0025-5416\(84\)90201-5](https://doi.org/10.1016/0025-5416(84)90201-5)
50. M.A. Martorano, C. Beckermann, and C.-A. Gandin, A Solutal Interaction Mechanism for the Columnar-to-Equiaxed Transition in Alloy Solidification, *Metall. Mater. Trans. A*, 2003, **34**(8), p 1657–1674. <https://doi.org/10.1007/s11661-003-0311-x>
51. S. Anandan, S. Pityana, and J. Dutta Majumdar, Structure-Property-Correlation in Laser Surface Alloyed AISI 304 Stainless Steel with WC+Ni+NiCr, *Mater. Sci. Eng. A*, 2012, **536**, p 159–169. <https://doi.org/10.1016/j.msea.2011.12.095>
52. H. Ali, H. Ghadbeigi, and K. Mumtaz, Processing Parameter Effects on Residual Stress and Mechanical Properties of Selective Laser Melted Ti6Al4V, *J. Mater. Eng. Perform.*, 2018, **27**(8), p 4059–4068.
53. H. Savaloni, E. Agha-Taheri, and F. Abdi, On the Corrosion Resistance of AISI 316L-Type Stainless Steel Coated with Manganese and Annealed with Flow of Oxygen, *J. Theor. Appl. Phys.*, 2016, **10**(2), p 149–156.
54. G. Abbas, Z. Liu, and P. Skeldon, Corrosion Behaviour of Laser-Melted Magnesium Alloys, *Appl. Surf. Sci.*, 2005, **247**(1), p 347–353. <https://doi.org/10.1016/j.apsusc.2005.01.169>
55. A. Biswas, L. Li, T.K. Maity, U.K. Chatterjee, B.L. Mordike, I. Manna and J. Dutta Majumdar, Laser Surface Treatment of Ti-6Al-4V for Bio-Implant Application, *Lasers Eng.*, 2007, **17**(1–2), p 59–73.
56. H.-B. Wu, T. Wu, T. Li, R.-Y. Sun, and Y. Gu, Effect of the Frequency of High-Angle Grain Boundaries on the Corrosion Performance of 5 wt.%Cr Steel in a CO₂ Aqueous Environment, *Int. J. Miner. Metall. Mater.*, 2018 <https://doi.org/10.1007/s12613-018-1575-x>
57. M. Vishnukumar, V. Muthupandi, and S. Jerome, Effect of Post-Heat Treatment on the Mechanical and Corrosion Behaviour of SS316L Fabricated by Wire Arc Additive Manufacturing, *Mater. Lett.*, 2022, **307**, p 131015.

Publisher's Note Springer Nature remains neutral with regard to jurisdictional claims in published maps and institutional affiliations.

Springer Nature or its licensor (e.g. a society or other partner) holds exclusive rights to this article under a publishing agreement with the author(s) or other rightsholder(s); author self-archiving of the accepted manuscript version of this article is solely governed by the terms of such publishing agreement and applicable law.